Geosci. Instrum. Method. Data Syst., 15, 335–355, 2026
https://doi.org/10.5194/gi-15-335-2026
© Author(s) 2026. This work is distributed under
the Creative Commons Attribution 4.0 License.

Geoscientific Instrumentation Methods and Data Systems
Open Access
EGU

Monitoring-informed scenario forecasting of spatial seismic demand for proactive resilience in the İzmir basin

Şahin Çağlar Tuna

Department of Civil Engineering, Yasar University, İzmir, Turkey

Correspondence: Şahin Çağlar Tuna (tunasahincaglar@gmail.com)

Received: 17 July 2026 – Discussion started: 10 August 2026
Revised: 25 October 2026 – Accepted: 3 November 2026 – Published: 23 November 2026

Abstract. Recorded seismic observations from monitoring networks provide a direct empirical basis for updating regional representations of earthquake demand, yet their use in scenario forecasting and proactive resilience planning remains limited. This study proposes a monitoring-informed sense–forecast–adapt workflow for forecasting spatial seismic demand in the İzmir Basin, western Türkiye. The framework transforms accumulated strong-motion records into a regional residual correction layer, embeds this layer within active-fault-based earthquake scenarios, and translates the resulting demand fields into adaptation-oriented spatial indicators.

A transparent reference ground-motion representation is first fitted using event magnitude, source-to-site distance, and site-condition information. Event–station residuals are then aggregated at the station level and interpolated to construct monitoring-informed residual and residual-variability fields. These updating layers are embedded within five representative active-fault scenarios around the İzmir Basin to generate baseline and monitoring-updated PGA fields. The resulting demand fields are evaluated through persistence, scenario sensitivity, monitoring priority, rank variability, and spatial concentration of high-demand domains.

The workflow is evaluated through residual-field validation, Gaussian-process benchmarking, robustness analyses, cumulative model-version tracking, and Monte Carlo uncertainty propagation. The results identify the Tuzla Fault scenario as the dominant demand case and the Yenifoça Fault scenario as the main secondary case. High-demand zones organize into spatially coherent regions, several locations remain repeatedly critical across multiple source scenarios, and the virtual regional demand representation stabilizes as the monitoring archive expands from 1977–2010 to 1977–2025.

The main contribution is an updateable forecasting workflow that integrates monitoring-derived residual updating, scenario-based spatial demand simulation, uncertainty-aware exceedance mapping, and resilience-oriented decision indicators. By transforming accumulated strong-motion observations into an evolving regional demand representation, the proposed framework moves beyond pointwise ground-motion estimation and provides a digital-twin-oriented basis for proactive seismic resilience planning in monitored basin environments.

1 Introduction

Earthquake effects are commonly interpreted through pointwise ground-motion estimates, although seismic demand is inherently spatial and is influenced by geological heterogeneity, basin structure, source-to-site configuration, and local site conditions. In sedimentary basins, these factors produce spatially coherent shaking patterns that cannot be fully represented by isolated station-level estimates. Consequently, regional resilience planning requires not only the prediction of shaking intensity at individual locations but also the identification of how elevated demand is organized across space, how it changes under alternative earthquake scenarios, and which areas remain consistently critical. Strong-motion monitoring networks provide an empirical basis for constructing and progressively refining such regional representations of spatial seismic demand.

Foundational studies established the probabilistic framework for conditional simulation of ground-motion fields at uninstrumented locations using correlation-consistent prediction and Kriging-based estimators (Vanmarcke and Fen-

ton, 1991; Vanmarcke et al., 1993), while more recent studies employed Gaussian-process regression to estimate ground-motion fields at locations without observations (Tamhidi et al., 2022). Operational systems such as ShakeMap further demonstrated the practical value of combining recorded motions, empirical prediction models, and spatially correlated residuals to produce event-specific shaking maps (Worden et al., 2010). Collectively, these studies established the importance of monitoring observations as constraints on spatial ground-motion fields.

A related body of work has focused on the spatial correlation of ground-motion residuals and its implications for regional hazard and risk assessment. Previous studies showed that intra-event residuals exhibit strong spatial dependence and that neglecting this dependence may bias regional hazard and portfolio-loss estimates (Goda and Atkinson, 2009; Loth and Baker, 2013). Region-specific correlation models (Huang and Wang, 2015) further demonstrated that sedimentary environments may generate characteristic spatial demand patterns that differ from generic regional assumptions. However, these studies have primarily addressed event-specific conditioning, correlation modelling, or post-event field reconstruction rather than repeatedly updating a regional demand representation for future scenario forecasting.

Bayesian updating studies provide another important foundation. Instrumental observations have been incorporated into regional probabilistic seismic hazard assessment (Viallet et al., 2019), while post-event regional analyses have shown that recorded motions reduce uncertainty in spatial hazard representations (Du and Padgett, 2021). Similar updating concepts have also been applied to regional liquefaction modelling and intensity-map refinement using newly available observations (Engler et al., 2025; Kwak and Ahn, 2026). These developments demonstrate the value of observation-informed updating but remain largely focused on post-event estimation rather than scenario-based forecasting.

A complementary perspective originates from structural health monitoring and digital twins. Recent predictive digital-twin frameworks emphasize continuous sensing, model updating, uncertainty quantification, forecasting, and decision support as components of a unified information loop (Torzoni et al., 2024). Broader reviews similarly identify physical-to-virtual information transfer, uncertainty propagation, and adaptive decision-making as defining characteristics of digital-twin systems (Thelen et al., 2022, 2023). Although these concepts have primarily been developed for individual structures, the same information flow can be extended to regional seismic monitoring by treating accumulated observations as a continuously updated representation of spatial seismic demand.

Accordingly, this study develops a monitoring-informed sense–forecast–adapt framework for basin-scale seismic-demand forecasting in the İzmir Basin, western Türkiye. Accumulated strong-motion observations are first converted into residual information relative to a transparent reference ground-motion representation. Station-level residual statistics are then transformed into spatial correction layers and combined with five representative active-fault scenarios – the İzmir Fault, Seferihisar Fault, Tuzla Fault, Gülbahçe Fault Zone, and Yenifoça Fault – to generate baseline and monitoring-updated PGA fields. Beyond deterministic demand mapping, the framework derives persistence, scenario sensitivity, monitoring priority, rank variability, and spatial concentration indicators. The residual field is evaluated using leave-one-station-out validation and Gaussian-process benchmarking, while the robustness of the proposed indicators is examined through threshold sensitivity, weighting sensitivity, and Monte Carlo uncertainty propagation.

To investigate the updateability of the framework, a digital-twin-oriented model-version experiment is further introduced. Cumulative monitoring archives covering 1977–2010, 1977–2015, 1977–2020, and 1977–2025 are used to regenerate the reference model, spatial residual field, scenario forecasts, and adaptation indicators. This enables the evolution of the regional virtual demand representation to be quantified as new monitoring records become available.

The study addresses four principal questions:

1. How can accumulated strong-motion observations be transformed into a monitoring-informed regional residual correction layer?

2. How do monitoring-updated spatial demand fields differ under alternative active-fault scenarios?

3. How stable and informative are persistence, scenario sensitivity, monitoring priority, and spatial concentration indicators for resilience planning?

4. How does the regional virtual demand representation evolve as the monitoring archive expands over time?

The resulting workflow transforms regional strong-motion observations from retrospective measurements into an updateable forecasting layer capable of supporting scenario comparison, uncertainty-aware interpretation, and adaptation-oriented decision making. In doing so, the study provides a field-based and digital-twin-oriented framework for proactive seismic resilience planning in monitored basin environments.

2 Study Area, Monitoring Dataset and Scenario Sources

The study focuses on the İzmir Basin and its surrounding seismotectonic region in western Türkiye. İzmir is located within an active extensional tectonic setting and is influenced by several mapped active fault systems in and around the metropolitan area. At the broader Eastern Mediterranean scale, western Türkiye lies within the western part of a proposed deep quasi-ring mantle structure centred beneath the

Cyprus region, whose surface projection is interpreted as exhibiting a predominantly counterclockwise rotational pattern (Eppelbaum et al., 2021). This regional interpretation was subsequently developed using additional magnetic-field, paleobiogeographic, and seismic-tomography evidence (Eppelbaum et al., 2025). The combination of active seismic sources, basin-controlled site conditions, and spatially distributed strong-motion observations makes the region a suitable test case for monitoring-informed forecasting of spatial seismic demand. In this study, the İzmir Basin is treated as a regional spatial domain in which earthquake demand may vary, concentrate, and shift under different source scenarios, rather than as a collection of isolated recording stations.

The overall workflow of the study is illustrated in Fig. 1. The framework follows a sense–forecast–adapt logic. In the sensing stage, recorded strong-motion observations are used to derive residual information relative to a reference ground-motion representation. In the forecasting stage, this monitoring-informed regional demand representation is combined with active-fault-based earthquake scenarios to generate baseline and updated spatial seismic demand fields. In the adaptation stage, the resulting forecasts are interpreted through resilience-oriented indicators, including persistent high-demand zones, scenario-sensitive demand shifts, spatial concentration of high-demand domains, monitoring priority, and rank stability of critical areas.

The monitoring dataset consists of 37 130 event–station records obtained from 119 strong-motion stations. The records correspond to 2980 earthquake events spanning the period 1977–2025. The magnitude range of the catalogue is approximately M2.2–7.6. The full event catalogue extends beyond the İzmir metropolitan area and provides a broader regional basis for residual construction, whereas the i˙-focused subset is used to support basin-scale interpretation and scenario forecasting. A practical İzmir subset defined by station identifiers beginning with 35 contains 15 639 event–station records from 39 stations and 1379 events.

Following data-quality screening, 53 records were excluded from reference-model fitting: 33 lacked a usable horizontal PGA component, 19 contained a non-positive horizontal PGA component, and one lacked magnitude information. The resulting modelling dataset therefore contained 37 077 usable event–station records.

For each event–station record, the two horizontal PGA components are combined using their geometric mean and used as the primary intensity measure in the analysis. Site-condition information is represented by station-level V_{s30}. The event magnitude, epicentral distance, depth, and V_{s30} are used to construct a transparent reference ground-motion representation, while the residuals between observed and predicted logarithmic PGA values provide the empirical basis for monitoring-informed spatial updating.

A regional active fault inventory (Emre et al., 2018) is used to define the seismotectonic context of the study area and to support the selection of representative earthquake scenarios. The active fault database contains mapped fault traces in geographic coordinates. The spatial distribution of monitoring stations, recorded event epicentres, mapped active faults, and selected scenario sources is shown in Fig. 2.

For scenario-based forecasting, a subset of active faults located around the İzmir Basin is selected as representative source configurations. These scenarios are not intended to reproduce specific historical earthquakes. Rather, they are used to examine how spatial seismic demand may change under alternative physically interpretable source conditions. The selected scenarios include the İzmir Fault, Seferihisar Fault, Tuzla Fault, Gülbahçe Fault Zone, and Yenifoça Fault. Each scenario is defined by a mapped fault trace, an assigned moment magnitude, and a representative source depth. These scenario sources are summarized in Table 1.

The assigned scenario magnitudes represent rounded, physically plausible rupture magnitudes informed by mapped fault or representative segment lengths, fault mechanisms, and empirical magnitude–rupture-length scaling relationships (Wells and Coppersmith, 1994).

The monitoring observations and the scenario source definitions are used for complementary purposes in the study. The recorded event–station observations provide the empirical basis for residual construction and regional demand updating, while the selected active-fault scenarios provide the source configurations for forward forecasting of spatial seismic demand. This structure links observed ground-motion data, regional active source conditions, and resilience-oriented interpretation within a single monitoring-informed forecasting framework.

3 Methodological Framework

3.1 Monitoring-Informed Residual Updating

The first stage of the framework converts recorded strong-motion observations into an observation-informed residual representation of regional seismic demand. Peak ground acceleration is used as the primary intensity measure, and the two horizontal components are combined using the geometric mean:

$$\mathrm{PGA_H} = \sqrt{\mathrm{PGA_{NS}} \times \mathrm{PGA_{EW}}}$$

where $\mathrm{PGA_{NS}}$ and $\mathrm{PGA_{EW}}$ are the two recorded horizontal components. This horizontal intensity measure is used consistently in the residual construction, spatial updating, and scenario forecasting stages. Station-level site effects are represented using V_{s30}, which is available for the monitoring stations and provides a practical site-condition descriptor for regional ground-motion analysis.

The logarithmic form of the horizontal intensity measure is used in the residual analysis:

$$y_{ij}^{\mathrm{obs}} = \ln(\mathrm{PGA_{H},}_{ij})$$

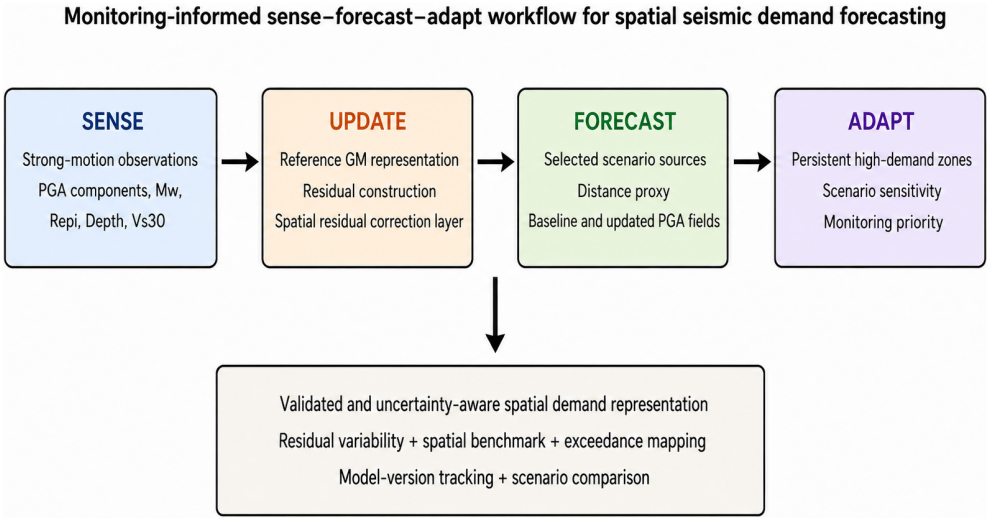


Figure 1. Sense–Forecast–Adapt workflow for monitoring-informed scenario forecasting of spatial seismic demand.

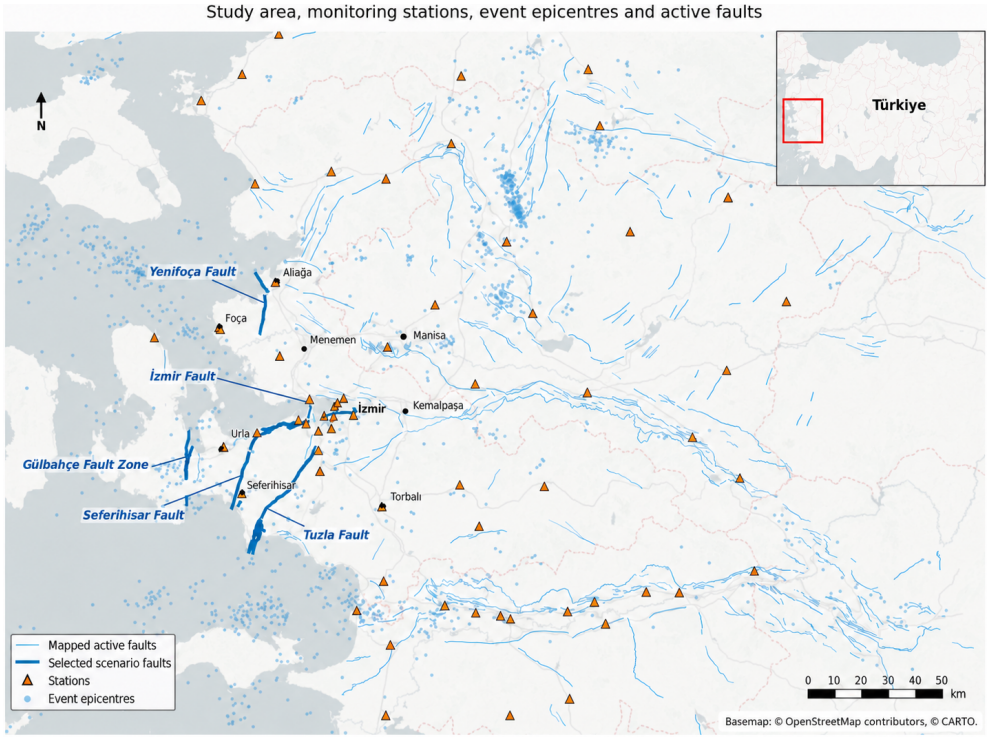


Figure 2. Study area, monitoring stations, recorded event epicentres, mapped active faults, and selected scenario faults.

where i denotes the monitoring station and j denotes the earthquake event. A transparent reference ground-motion representation is then used to estimate the expected logarithmic PGA for each event–station pair:

$$y_{ij}^{\text{pred}} = f\left(M_j, R_{ij}, V_{\text{s30},i}\right)$$

where M_j is the event magnitude, R_{ij} is the event-to-station distance measure, and $V_{\text{s30},i}$ is the station-level site-condition descriptor. In the present implementation, the reference representation is fitted in logarithmic PGA space using magnitude, effective distance terms, and normalized V_{s30}. The effective distance is defined as:

$$R_{\text{eff},ij} = \sqrt{{R_{\text{epi},ij}}^2 + {h_j}^2}$$

where $R_{\text{epi},ij}$ is the epicentral distance and h_j is the event depth. The reference representation was fitted using Huber

Table 1. Selected earthquake scenarios used for spatial demand forecasting.

Scenario	Source	M_w	Depth (km)	Purpose in the analysis
S1	İzmir Fault	6.5	10	Near-basin source scenario
S2	Seferihisar Fault	6.6	10	Southwestern source scenario
S3	Tuzla Fault	7	10	High-magnitude southern source scenario
S4	Gülbahçe Fault Zone	6.6	10	Western source scenario
S5	Yenifoça Fault	6.8	10	Northwestern source scenario

regression with standardized predictors. Its functional form is:

$$\ln(\text{PGA_H}) = \beta_0 + \beta_1 M + \beta_2 \ln(R_{\text{eff}}) + \beta_3 R_{\text{eff}} + \beta_4 \ln(V_{s30}/760)$$

and the fitted coefficients, expressed in the original predictor scales, give:

$$\ln(\text{PGA_H}) = -1.6648 + 1.6252M - 1.2441\ln(R_{\text{eff}}) - 0.00427R_{\text{eff}} - 0.4474\ln(V_{s30}/760)$$

Here, R_{eff} is expressed in km and V_{s30} in m s^{-1}. Huber regression was adopted to reduce the influence of extreme ground-motion observations while retaining a transparent parametric reference representation. The reference model is not intended to replace a full ground-motion prediction equation; rather, it provides a consistent baseline against which monitoring residuals can be constructed.

The event–station residual is computed as:

$$r_{ij} = y_{ij}^{\text{obs}} - y_{ij}^{\text{pred}}$$

or equivalently,

$$r_{ij} = \ln\left(\text{PGA}_{\text{H},ij}^{\text{obs}}\right) - \ln(\text{PGA}_{\text{H},ij}^{\text{pred}})$$

Positive residuals indicate stronger-than-expected shaking relative to the reference representation, whereas negative residuals indicate weaker-than-expected shaking. The residuals are then aggregated at the station level to obtain a monitoring-informed residual tendency:

$$\bar{r}_i = \frac{1}{n_i}\sum_{j=1}^{n_i} r_{ij}$$

where n_i is the number of usable records at station i. The value $\bar{r}_i$ represents the average deviation of recorded motions at a station from the reference prediction and is used as an observation-derived correction term for regional demand updating.

The variability of residuals at each station is also evaluated as:

$$s_{\text{r},i} = \sqrt{\frac{1}{n_i - 1}\sum_{j=1}^{n_i}(r_{ij} - \bar{r}_i)^2}$$

The station residual standard deviation $s_{\text{r},i}$ characterizes event-to-event variability, while the precision of the station-mean residual is represented by its standard error, $\text{SE}(\bar{r}_i) = \frac{s_{\text{r},i}}{\sqrt{n_i}}$

As a sensitivity check, event-specific mean residuals were removed for earthquakes recorded at two or more stations. Event-centered residuals were defined as

$$r_{ij}^{*} = r_{ij} - \bar{r}_{\text{event},j}$$

and were subsequently aggregated at the station level and interpolated using the same IDW procedure as the baseline residual field. The resulting correction and scenario-output fields were compared with the baseline results.

Stations with at least 10 usable records were retained for the baseline spatial update. The robustness of this criterion was additionally evaluated using minimum-record thresholds of 20, 30, 50, and 100 records per station.

To extend the residual information from monitoring stations to the regional prediction grid, the station-level residuals are converted into a spatial residual correction field:

$$r_{\text{s}}(x) = I(\bar{r}_1, \bar{r}_2, \ldots, \bar{r}_N; x)$$

where x denotes a prediction location, N is the number of monitoring stations used for spatial updating, and $I(\cdot)$ is the spatial interpolation operator. In the baseline implementation, inverse-distance weighting was performed in UTM Zone 35N (EPSG:32635) using an inverse-distance power of 2 and the eight nearest available stations. No fixed search radius was imposed. A regular 2 km prediction grid was constructed over the study domain (26.55–27.45° E and 38.05–38.80° N). The same interpolation settings were used for the residual correction, residual-variability, and station-informed V_{s30} fields.

To evaluate whether the spatial residual correction layer provides meaningful out-of-station information, a leave-one-station-out cross-validation procedure is applied. In each validation step, one monitoring station is removed, the residual correction surface is reconstructed using the remaining stations, and the residual at the omitted station is predicted. The observed and predicted station residuals are then compared using the RMSE, MAE and Bias metrics. For benchmarking, the same leave-one-station-out predictions were also compared with no residual correction, a leave-one-out global-

mean residual correction, and a nearest-station residual correction.

To evaluate spatial transferability under larger monitoring gaps, a six-block spatial cross-validation was performed. Spatially grouped stations were withheld simultaneously, and their residual tendencies were predicted from the remaining monitoring network using the same IDW procedure.

Generalization to previously unseen earthquakes was further evaluated using five-fold grouped-event validation. All records belonging to the same earthquake were assigned to the same fold, ensuring that test events were not represented during model fitting. For each fold, the reference model and spatial residual correction field were reconstructed using only the training events, and performance was evaluated against station-level residual tendencies derived from the held-out events.

A Gaussian-process residual surface was also fitted as a covariance-based benchmark. The GP used a constant × radial-basis-function kernel with an additional white-noise term, with an initial correlation length of 15 km and bounds of 1–200 km. The response was normalized and kernel hyperparameters were optimized using three optimizer restarts. IDW was retained as the primary updating method because it provides a transparent, deterministic, and readily reproducible interpolation operator that can be applied consistently across successive model versions; the GP was used as an independent benchmark rather than as the primary forecasting surface.

3.2 Scenario-Based Spatial Demand Forecasting

The second stage uses active-fault-based earthquake scenarios to generate spatial seismic demand forecasts. Each scenario is represented by:

$$S_k = \{M_{\mathrm{w},k}, \mathrm{Faulttrace}_k, h_k\}$$

where $M_{\mathrm{w},k}$ is the assigned scenario magnitude, $\mathrm{FaultTrace}_k$ is the mapped fault trace, and h_k is the representative source depth.

For scenario-based forecasting, source-to-site distance is computed from the mapped scenario fault traces. Distance-to-source measures are fundamental inputs in empirical ground-motion prediction and regional seismic-demand modelling, and alternative definitions may be adopted depending on the source representation and the objective of the analysis (Kaklamanos et al., 2011; Campbell and Bozorgnia, 2014). In this study, the primary horizontal source-distance measure is defined as the shortest distance from a station or prediction location x to the corresponding scenario fault trace:

$$R_{\mathrm{trace},k}(x) = \min d_{\mathrm{horizontal}}(x, \mathrm{Faulttrace}_k)$$

To incorporate the representative scenario depth, a depth-adjusted source-distance metric is calculated as

$$R_{\mathrm{proxy},k}(x) = \sqrt{R_{\mathrm{trace},k}(x)^2 + {h_k}^2}$$

where $h_{\mathrm{k}} = 10$ km for the selected scenarios. For the scenario calculations, source-to-site distance was defined using the shortest horizontal distance to the mapped fault trace combined with the representative source depth. This formulation provides a consistent distance measure for comparison among the selected scenarios. Sensitivity to the assumed source depth was examined using values of 5, 10, and 15 km.

This metric is used consistently across all scenario sources to generate comparable spatial seismic demand forecasts.

For each scenario k, the baseline logarithmic PGA field is computed as

$$y_k^{\mathrm{base}}(x) = f\left(M_{\mathrm{w},k}, R_{\mathrm{proxy},k}(x), V_{\mathrm{s30}}(x)\right)$$

where $V_{\mathrm{s30}}(x)$ is the station-informed spatial site-condition field. The corresponding baseline PGA value is obtained as:

$$\mathrm{PGA}_k^{\mathrm{base}}(x) = \exp\left(y_k^{\mathrm{base}}(x)\right)$$

The monitoring-informed updated forecast is obtained by adding the spatial residual field to the baseline scenario demand:

$$y_k^{\mathrm{upd}}(x) = y_k^{\mathrm{base}}(x) + r_{\mathrm{s}}(x) \text{ and } \mathrm{PGA}_k^{\mathrm{upd}}(x) = \exp(y_k^{\mathrm{upd}}(x)).$$

This updated field combines the scenario source condition, reference ground-motion representation, site-condition descriptor, and observation-derived residual correction. The difference between the updated and baseline demand fields is expressed as a demand escalation index:

$$\mathrm{DEI}_k(x) = y_k^{\mathrm{upd}}(x) - y_k^{\mathrm{base}}(x)$$

Because the updating is additive in logarithmic space, $\mathrm{DEI_k}(x)$ is equivalent to the spatial residual correction applied to the baseline scenario field. Positive values indicate locations where monitoring-informed updating increases forecasted demand relative to the baseline scenario field.

3.3 Adaptation-Oriented Forecast Indicators

The third stage translates the forecasted demand fields into indicators that support proactive resilience planning. These indicators are not intended to represent direct damage or loss estimates. Instead, they identify areas where forecasted seismic demand is elevated, persistent, scenario-sensitive, spatially concentrated, or associated with higher updating uncertainty.

For a selected demand threshold $\mathrm{PGA_c}$, the high-demand domain under scenario k is defined as:

$$H_k(x) = \begin{cases} 1, & \mathrm{PGA}_k^{\mathrm{upd}}(x) \geq \mathrm{PGA_c} \\ 0, & \mathrm{PGA}_k^{\mathrm{upd}}(x) < \mathrm{PGA_c} \end{cases}$$

The high-demand threshold, PGA_c, is defined as the 80th percentile of all monitoring-updated PGA values pooled across the five scenario fields and all prediction-grid locations. This percentile-based definition identifies the upper-demand portion of the scenario ensemble and provides a common threshold for persistence, connected-domain, and exceedance-probability analyses.

Because the threshold is defined from the pooled 80th percentile of all scenario-grid values, the domain-averaged persistence is approximately 0.20 by construction. Accordingly, persistence is interpreted primarily through its spatial distribution and maximum values rather than through its domain mean.

The persistence of high-demand behavior across all scenarios is then quantified as:

$$P(x) = \frac{1}{K}\sum_{k=1}^{K} H_k(x)$$

where K is the number of earthquake scenarios. Values of $P(x)$ close to 1 indicate locations that repeatedly fall within high-demand zones across multiple scenarios.

Scenario sensitivity is evaluated from the variability of updated logarithmic PGA forecasts across the scenario set:

$$\mathrm{SS}(x) = \mathrm{std}\left(y_1^{\mathrm{upd}}(x), y_2^{\mathrm{upd}}(x), \ldots, y_K^{\mathrm{upd}}(x)\right)$$

High values of $\mathrm{SS}(x)$ indicate locations where the forecasted demand is strongly controlled by the selected earthquake source.

A Monitoring Priority Indicator (MPI) is defined by combining normalized forecasted demand and normalized residual variability. MPI is intended as a demand-side screening indicator for identifying locations where intensified monitoring or more detailed site-specific evaluation may be warranted; it does not represent a complete inspection-priority or risk metric.

$$\tilde{y}_{\mathrm{upd}}(x) = \frac{\bar{y}_{\mathrm{upd}}(x) - \min(\bar{y}_{\mathrm{upd}})}{\max(\bar{y}_{\mathrm{upd}}) - \min(\bar{y}_{\mathrm{upd}})}$$

$$\sigma_{\mathrm{s}}(x) = \frac{\sigma_{\mathrm{s}}(x) - \min(\sigma_{\mathrm{s}})}{\max(\sigma_{\mathrm{s}}) - \min(\sigma_{\mathrm{s}})}$$

$$\mathrm{MPI}(x) = 0.60 \times \tilde{y}_{\mathrm{upd}}(x) + 0.40 \times \sigma_{\mathrm{s}}(x)$$

Both components are independently rescaled to [0,1] using min–max normalization over the prediction grid before applying the MPI weights. High MPI values identify locations where elevated demand and higher residual variability coincide, making them candidates for intensified monitoring or more detailed site-specific assessment.

Finally, grid points are ranked according to their updated demand values under each scenario. The variability of these ranks across scenarios is used to evaluate whether a location remains consistently important or whether its relative criticality changes with the assumed source configuration. Rank-stable locations remain high-priority across scenarios, whereas high rank-variability locations are interpreted as source-sensitive.

3.4 Robustness, Uncertainty Propagation and Model-Version Tracking

Beyond the baseline scenario forecasts and adaptation-oriented indicators, a series of analyses are conducted to evaluate the stability, uncertainty, and updateability of the proposed workflow. These analyses are designed to test whether the spatial indicators depend strongly on threshold selection or priority-index weighting, whether high-demand domains form coherent spatial structures, how residual variability affects exceedance interpretation, and how the monitoring-informed representation evolves as the strong-motion archive expands.

First, threshold sensitivity is evaluated by repeating the high-demand classification using multiple percentile-based and fixed PGA thresholds. The percentile thresholds include the 70th, 75th, 80th, 85th and 90th percentiles of all monitoring-updated scenario PGA values. Fixed thresholds of 150, 200 and 250 are also tested. For each threshold, the high-demand domains, persistence values and high-demand grid fractions are recalculated. This provides a robustness check on whether persistent demand patterns are specific to a single threshold or remain visible under alternative demand definitions.

Second, the sensitivity of the Monitoring Priority Indicator (MPI) to the weighting scheme is evaluated. The baseline MPI uses a demand-dominant weighting of $w_1 = 0.60$ and $w_2 = 0.40$, where w_1 is assigned to normalized updated demand and w_2 to normalized residual variability. To test the stability of the priority structure, the following alternative weight combinations are considered: $(w_1, w_2) \in \{(0.80, 0.20), (0.60, 0.40), (0.50, 0.50), (0.40, 0.60), (0.20, 0.80)\}$.

The resulting MPI rankings are compared with the baseline configuration using Spearman rank correlation and top-10 % priority overlap. This test evaluates whether monitoring-priority regions remain stable under alternative planning preferences.

Magnitude-range sensitivity is evaluated by refitting the complete workflow using records with $M \geq 4.0$, $M \geq 4.5$, and $M \geq 5.0$. The resulting reference models, spatial residual fields, scenario forecasts, and persistence patterns are compared with the full-catalogue results to assess the influence of the magnitude composition of the calibration dataset.

Third, the spatial concentration of high-demand domains is evaluated using connected-component analysis. For each scenario and threshold, the binary high-demand field is con-

verted into connected regions on the prediction grid. Connected components are identified using four-neighbour grid connectivity, such that high-demand cells are considered connected only when they share a horizontal or vertical grid edge; diagonal adjacency is not treated as a connection. The number of connected components, high-demand grid fraction, largest component size, largest component ratio and component fragmentation are computed. These metrics distinguish spatially coherent high-demand domains from fragmented or isolated exceedance patterns.

For uncertainty-aware spatial interpretation, the residual-variability field is used to characterize event-to-event residual dispersion, while the Gaussian-process prediction standard deviation represents spatial prediction uncertainty. These components are combined in quadrature to define the predictive-dispersion field:

$$\sigma_{\mathrm{pred}}(x) = \sqrt{\sigma_{\mathrm{s}}(x)^2 + \sigma_{\mathrm{GP}}(x)^2}$$

where $\sigma_{\mathrm{s}}(x)$ is the interpolated residual-variability field and $\sigma_{\mathrm{GP}}(x)$ is the Gaussian-process prediction standard deviation. For each grid point and scenario, Monte Carlo realizations are generated as:

$$Y_k^{\mathrm{mc}}(x) = y_k^{\mathrm{base}}(x) + r_{\mathrm{s}}(x) + \epsilon(x)$$

where:

$$\epsilon(x) \sim N\left(0, \sigma_{\mathrm{s}}(x)^2\right)$$

Monte Carlo perturbations were sampled independently at individual grid locations conditional on the local predictive-dispersion value; no additional spatial covariance was imposed between grid cells. Accordingly, the resulting exceedance probabilities are interpreted as pointwise uncertainty measures rather than as realizations of a spatially correlated ground-motion random field.

$$\mathrm{PGA}_k^{\mathrm{MC}}(x) = \exp\left(Y_k^{\mathrm{MC}}(x)\right)$$

The exceedance probability for the selected threshold $\mathrm{PGA_c}$ is then computed as:

$$P_{\mathrm{exc},k}(x) = \frac{1}{N_{\mathrm{MC}}} \sum_{m=1}^{N_{\mathrm{MC}}} I\left(\mathrm{PGA}_{k,m}^{\mathrm{MC}}(x) \geq \mathrm{PGA_c}\right)$$

where N_{MC} is the number of Monte Carlo realizations and $I(\cdot)$ is the indicator function. This produces scenario-specific exceedance-probability maps and summary measures such as mean exceedance probability, maximum exceedance probability, and the fraction of grid points with exceedance probability greater than selected probability levels.

Finally, a cumulative model-version tracking experiment is performed to evaluate how the monitoring-informed regional demand representation evolves as new records become available. The event catalogue is divided into cumulative model versions according to the end years 2010, 2015, 2020 and 2025. Each version includes all usable records up to the corresponding end year:

$$D_v = \{d_j : \mathrm{year}_j \leq Y_v\}$$

where D_v is the cumulative dataset for model version v and Y_v is the corresponding end year. For each model version, the reference ground-motion representation is refitted, event–station residuals are recalculated, station-level residual tendencies are reconstructed, and a new spatial residual correction layer is generated. The scenario forecasts and adaptation-oriented indicators are then regenerated for each version.

To distinguish the contribution of archive growth from monitoring-network expansion, a fixed-network sensitivity analysis was performed using the same 19 stations that satisfied the spatial-update criterion in the earliest model version and remained available throughout all subsequent versions. The model-version sequence was regenerated using this common station set.

Sequential update metrics are computed between consecutive model versions. For two consecutive versions $v-1$ and v, the residual-field change is quantified as:

$$\Delta r_{\mathrm{s}}^{\mathrm{RMSE}} = \sqrt{\frac{1}{G}\sum_{g=1}^{G}\left[r_{\mathrm{s},v} \times (g) - r_{\mathrm{s},v-1} \times (g)\right]^2}$$

where G is the number of grid points. Similarly, the change in the monitoring-priority indicator is quantified as:

$$\Delta\mathrm{MPI}^{\mathrm{RMSE}} = \sqrt{\frac{1}{G}\sum_{g=1}^{G}\left[\mathrm{MPI}_v \times (g) - \mathrm{MPI}_{v-1} \times (g)\right]^2}$$

The Spearman rank correlation between consecutive MPI fields and the overlap of the top-10 % priority grid points are also computed. These metrics indicate whether updated monitoring records substantially modify the regional priority structure or whether the representation stabilizes as the archive becomes denser. The main methodological quantities used in the workflow are summarized in Table 2.

The following section applies this workflow to the İzmir Basin monitoring dataset and the five selected scenario sources defined in Sect. 2. The results are presented in the same sequence as the methodological framework: first, the reference ground-motion representation and residual correction layer are evaluated; second, the spatial residual surface is validated and benchmarked; third, baseline and monitoring-updated scenario forecasts are compared; and finally, the adaptation-oriented indicators, robustness checks, model-version tracking and Monte Carlo exceedance-probability outputs are interpreted in terms of proactive resilience planning.

Table 2. Summary of methodological quantities used in the sense–forecast–adapt framework.

Quantity	Definition	Interpretation
$\mathrm{PGA_H}$	$\sqrt{\mathrm{PGA_{NS}} \times \mathrm{PGA_{EW}}}$	Geometric mean horizontal PGA
$\left(r_{\{ij\}}\right)$	$\left(y_{\{ij\}}^{\{\mathrm{obs}\}} - y_{\{ij\}}^{\{\mathrm{pred}\}}\right)$	Event–station residual
$(\overline{r_i})$	station mean residual	Station-level correction
$\mathrm{SE}(\bar{r}_i)$	$\mathrm{SE}(\bar{r}_i) = \frac{s_{\mathrm{r},i}}{\sqrt{n_i}}$	Sampling uncertainty of station-mean residual
$\left(r_{s(x)}\right)$	interpolated $(\overline{r_i})$	Spatial residual correction
$\left(\mathrm{PGA}_k^{\{\mathrm{upd}\}(x)}\right)$	$\left(\exp\left(y_k^{\{\mathrm{base}\}(x)} + r_{\mathrm{s}(x)}\right)\right)$	Updated scenario demand
$(P\,(x))$	$\frac{1}{K}\sum_{k=1}^{K} H_k(x)$	Persistence
$(\mathrm{SS}\,(x))$	$\left(\mathrm{std}\left(y_1^{\{\mathrm{upd}\}}, \ldots, y_K^{\{\mathrm{upd}\}}\right)\right)$	Scenario sensitivity
$(\mathrm{MPI}\,(x))$	$\left(w_{\tilde{1}\{y\}}^{\{\mathrm{upd}\}(x)} + w_{\tilde{2}\{\sigma\}_{s(x)}}\right)$	Monitoring Priority Indicator
$\sigma_{\mathrm{pred}}(x)$	$\sigma_{\mathrm{pred}}(x) = \sqrt{\sigma_{\mathrm{s}}(x)^2 + \sigma_{\mathrm{GP}}(x)^2}$	Predictive-dispersion field
$(P_{\mathrm{exc},k}\,(x))$	Monte Carlo exceedance probability	Uncertainty-aware exceedance indicator

4 Results

4.1 Reference Model, Residual Correction and Spatial Validation

The reference ground-motion representation was fitted using 37 077 usable event–station records obtained from 119 strong-motion stations and 2974 earthquake events. The model explains a substantial part of the logarithmic variability in horizontal PGA, with an R^2 value of 0.633. The logarithmic RMSE and MAE are 0.801 and 0.622, respectively. The mean residual is close to zero, indicating that the reference representation provides a balanced baseline at the dataset scale. The residual standard deviation is 0.800, reflecting the expected variability of regional ground-motion observations. The performance metrics are summarized in Table 3.

Table 3. Performance of the reference ground-motion representation.

Metric	Value
Number of usable records	37 077
Number of stations	119
Number of events	2974
(R^2), log scale	0.633
RMSE, log scale	0.801
MAE, log scale	0.622
Mean residual	0.025
Residual standard deviation	0.800

Before using the residuals as monitoring-informed updating quantities, the fitted reference model was examined for physical plausibility. This check is important because the residual correction layer is meaningful only if the reference model captures the main first-order controls on ground-motion intensity in a consistent manner. The scaled coefficients show the expected directional behavior: the magnitude term is positive, indicating larger predicted PGA for larger events, whereas the distance-related terms are negative, reflecting attenuation with increasing source-to-site distance. The V_{s30}-related coefficient is also negative, meaning that, within the fitted log-linear structure, stiffer site conditions are associated with lower predicted PGA. These coefficient signs indicate that the reference model provides a physically reasonable baseline for residual construction, although it is not intended to replace a full ground-motion prediction equation.

The event–station residuals were then aggregated at the station level and interpolated over the prediction domain. A total of 108 stations satisfied the minimum requirement of 10 usable records and were retained for spatial updating. The station-level mean residuals range from −0.790 to 2.867, with an average of 0.163 and a median of 0.122. Over the prediction grid, the interpolated residual field ranges from −0.786 to 0.537, with a mean value of −0.036 and a median value close to zero.

The median number of records per station was 323. Increasing the minimum-record requirement from 10 to 20, 30, or 50 records produced an unchanged spatial residual field, while a more restrictive 100-record threshold still

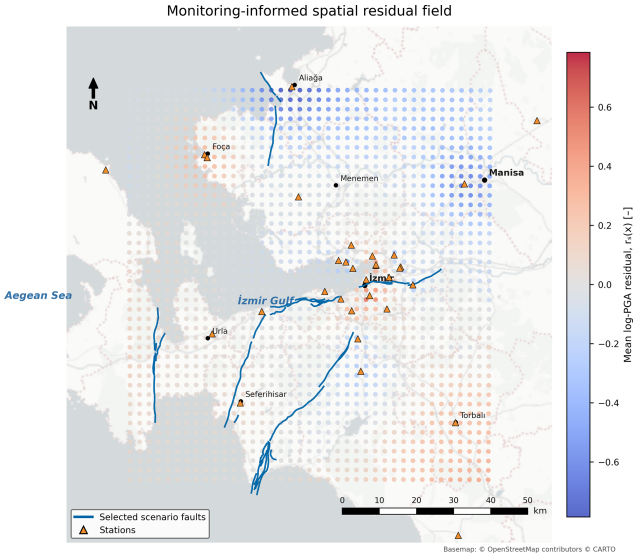


Figure 3. Monitoring-informed spatial residual field derived from station-level residuals.

yielded very high agreement with the baseline field (Pearson $r = 0.990$; Spearman $\rho = 0.981$; RMSE $= 0.025$ log units). The standard error of the station-mean residual decreased strongly with increasing record count (Spearman $\rho = -0.902$), confirming the expected increase in statistical reliability with station sample size.

In addition to the mean residual correction field, a residual-variability field was constructed by interpolating the station-level residual standard deviations over the same prediction grid. While the mean residual field provides the demand adjustment applied to the baseline scenario forecasts, the residual-variability field represents the spatial distribution of event-to-event residual dispersion. This variability field has a mean value of 0.663 and ranges from 0.553 to 0.955 over the grid. It is therefore used not as a direct PGA correction, but as the residual-dispersion component of the Monitoring Priority Indicator (MPI) and the Monte Carlo predictive-dispersion formulation.

To evaluate the spatial reliability of the residual correction layer, a leave-one-station-out diagnostic validation was performed. In this test, each station is omitted in turn, the residual surface is reconstructed using the remaining stations, and the residual tendency at the omitted station is predicted. The IDW residual surface was also compared with a Gaussian-process benchmark surface.

To place the spatial residual predictions in context, the leave-one-station-out validation also considered three simple reference cases: no residual correction, a global-mean residual correction, and a nearest-station correction. The corresponding validation metrics are summarized in Table 4.

The simple-baseline comparison confirms that station-level residual tendencies are difficult to predict precisely from spatial position alone. The no-correction and global-mean baselines yield RMSE values of 0.396 and 0.386, respectively, while nearest-station prediction performs less well (RMSE $= 0.474$). The Gaussian-process benchmark provides the lowest RMSE (0.379) and MAE (0.297), whereas IDW yields an RMSE of 0.405. These results indicate only modest pointwise predictive gain from spatial residual interpolation. Accordingly, the residual surface is interpreted primarily as a spatially varying regional correction layer rather than as a high-precision local residual predictor.

Table 4. Leave-one-station-out diagnostic validation and simple-baseline comparison of the spatial residual correction layer.

Method	RMSE	MAE	Bias	Spearman (ρ)
No correction	0.396	0.313	−0.103	–
Global mean	0.386	0.311	0.000	–
Nearest station	0.474	0.379	0.026	0.224
IDW	0.405	0.319	0.040	0.227
Gaussian process	0.379	0.297	0.002	0.166

The full GP fit yielded an optimized spatial correlation length of approximately 33.3 km. Although GP produced slightly lower cross-validated errors than IDW, IDW was retained as the baseline updating surface for methodological transparency and consistent regeneration across model versions rather than on the basis of superior local predictive accuracy.

The event-centered sensitivity analysis retained 36 254 records from 2428 multi-station events. The original and event-centered spatial residual fields remained highly consistent (Pearson $r = 0.976$; Spearman $\rho = 0.964$; RMSE $= 0.040$ log units). The resulting scenario PGA fields also remained nearly unchanged, with spatial correlations exceeding 0.997 for all five scenarios. MPI and persistence patterns were similarly stable, indicating that the main spatial correction structure is not materially controlled by event-specific mean residual effects.

The grouped-event validation further assessed generalization to earthquakes excluded from model fitting. Across five folds, the IDW correction reduced the RMSE of held-out station-level residual tendencies from 0.377 to 0.337 and the MAE from 0.301 to 0.261, corresponding to improvements of approximately 10.4 % and 13.4 %, respectively. Mean Pearson and Spearman correlations were 0.442 and 0.416. These results indicate transferable information on persistent station-level tendencies across previously unseen events.

The six-block spatial validation produced an RMSE of 0.402 and an MAE of 0.320, closely matching the leave-one-station-out values. Bias was 0.005, although Spearman correlation decreased to 0.050 when entire spatial groups were withheld. Prediction errors were also larger for stations located more than 20 km from the nearest available monitoring

station (RMSE = 0.447), indicating that local residual ranking becomes less reliable across larger monitoring gaps.

Magnitude-range sensitivity was also examined. Of the 37 077 modelling records, 17 402 (46.9 %) correspond to $M \geq 4.0$, 7944 (21.4 %) to $M \geq 4.5$, and 3631 (9.8 %) to $M \geq 5.0$. Refitting the complete workflow using these subsets preserved the scenario hierarchy and spatial demand patterns, with correlations exceeding 0.98 relative to the full-catalogue forecasts. Persistence patterns were also highly consistent. However, mean scenario PGA values increased by approximately 31 %–49 % in the moderate-to-large-event subset models, indicating that absolute demand levels remain sensitive to the magnitude range used for calibration.

4.2 Scenario-Based Spatial Demand Forecasts

The five representative active-fault scenario sources were used to generate baseline and monitoring-updated PGA forecasts over the prediction grid. The scenario sources were selected from mapped active fault systems around the İzmir Basin, consistent with national active-fault inventories and regional tectonic studies of the İzmir Gulf and surrounding fault zones (Emre et al., 2018; Coşkun et al., 2017; Özener et al., 2013; Şengöçmen Geçkin et al., 2021). For each scenario, the baseline field was computed using the assigned magnitude, the depth-adjusted source-distance proxy, and the station-informed V_{s30} field. The monitoring-updated field was then obtained by adding the spatial residual correction layer to the baseline logarithmic PGA field.

The scenario forecast summary is given in Table 5. The results show clear differences among the five source configurations. The Tuzla Fault scenario, S3, produces the highest mean monitoring-updated PGA, with a mean value of 367.10 and a maximum value of 1433.05. The Yenifoça Fault scenario, S5, produces the second highest mean updated PGA, with a mean value of 204.79 and a maximum value of 979.32. The İzmir Fault, Seferihisar Fault, and Gülbahçe Fault Zone scenarios produce lower mean updated PGA values, but still generate localized high-demand areas.

The comparison between baseline and monitoring-updated values in Table 5 demonstrates the hybrid nature of the forecast product. The baseline forecasts reflect the assigned magnitude, mapped source geometry, depth-adjusted distance structure, and station-informed site representation. The updated forecasts retain this source-controlled structure but modify the spatial demand levels according to the monitoring-derived residual correction layer. The residual update slightly reduces the mean PGA in S1, S3, and S5, while slightly increasing it in S2 and S4. This behavior reflects the spatial interaction between the source-controlled baseline field and the observation-derived correction layer. Overall, S3 remains the dominant scenario in both baseline and updated forms, indicating that the Tuzla Fault source configuration produces the broadest and strongest demand footprint among the selected scenarios.

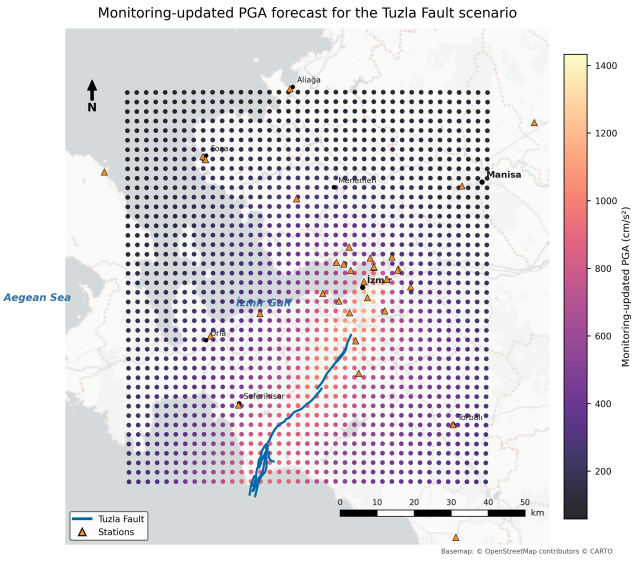


Figure 4. Monitoring-updated PGA forecast for the Tuzla Fault scenario.

The high-demand grid ratio further distinguishes the scenarios. Using the common p80 high-demand threshold, the Tuzla Fault scenario classifies 42.9 % of the grid as high demand, indicating the broadest spatial influence among the selected scenarios. The Yenifoça Fault scenario follows with 17.9 %. The İzmir Fault, Seferihisar Fault, and Gülbahçe Fault Zone scenarios produce high-demand grid ratios of 14.1 %, 13.7 %, and 11.4 %, respectively. These results show that the spatial extent of high-demand areas is strongly scenario-dependent.

The spatial distribution of the monitoring-updated PGA field for the Tuzla Fault scenario is shown in Figure 4. This scenario produces the highest mean and maximum updated PGA values among the five source configurations and therefore provides a representative example of the strongest scenario-controlled demand pattern. The map illustrates how the monitoring-updated demand field is not only controlled by the source geometry, but also shaped by the spatial residual correction layer derived from accumulated strong-motion observations.

The source-distance sensitivity analysis showed that changing the representative depth from 10 km to 5 or 15 km altered absolute PGA levels but had little effect on the spatial ordering of demand within each scenario. Spearman correlations with the baseline 10 km fields exceeded 0.997 in all cases, and the Tuzla Fault remained the dominant scenario. This indicates that the principal spatial interpretation is robust, although absolute demand levels remain dependent on the adopted source-depth representation.

Table 5. Summary of baseline and monitoring-updated PGA forecasts for the five selected scenario sources.

Scenario	Source	Mw	Mean baseline PGA ($cm\,s^{-2}$)	Max baseline PGA ($cm\,s^{-2}$)	Mean updated PGA ($cm\,s^{-2}$)	Max updated PGA ($cm\,s^{-2}$)	High-demand grid (%)
S1	İzmir Fault	6.5	197.13	770.46	188.69	843.83	14.1
S2	Seferihisar Fault	6.6	181.69	544.46	182.87	576.79	13.7
S3	Tuzla Fault	7	368.47	1563.1	367.1	1433.05	42.9
S4	Gülbahçe Fault Zone	6.6	144.62	562.18	146.95	599.78	11.4
S5	Yenifoça Fault	6.8	218.55	1055.47	204.79	979.32	17.9

Table 6. Summary of persistence, scenario sensitivity, and priority indicators.

Indicator	Value
High-demand threshold, (PGA_c)	334.26
Threshold mode	80th percentile
Number of grid points	1638
Mean persistence	0.2
Maximum persistence	0.8
Mean scenario sensitivity	0.487
Maximum scenario sensitivity	0.96
Mean monitoring priority indicator, MPI	0.419
Maximum monitoring priority indicator, MPI	0.937

4.3 Adaptation-Oriented Indicators and Robustness Checks

High-demand zones were identified using the 80th percentile of all updated scenario PGA values as the demand threshold. The threshold value and the resulting summary statistics for persistence, scenario sensitivity, and monitoring priority are reported in Table 6. For each scenario, grid points exceeding this value were classified as high-demand locations. The persistence indicator was then computed as the fraction of scenarios in which each grid point exceeded the threshold.

As expected from the pooled p80 threshold definition, the domain-averaged persistence is 0.200. The more informative result is the maximum persistence of 0.800, indicating that some locations exceed the common high-demand threshold in four of the five source scenarios. As shown in Fig. 5a, the spatial distribution of persistence identifies locations that remain repeatedly critical across alternative source configurations.

Scenario sensitivity was evaluated using the standard deviation of updated logarithmic PGA forecasts across the five scenarios. The mean scenario sensitivity is 0.487, and the maximum value is 0.960. Its spatial distribution is shown in Fig. 5b. In contrast to the persistence map, which highlights repeatedly critical zones, the scenario-sensitivity map identifies areas where forecasted demand changes strongly depending on the assumed earthquake source. These areas are important for what-if forecasting because they cannot be represented adequately by a single deterministic demand field.

The Monitoring Priority Indicator (MPI) combines normalized mean updated demand and normalized residual variability. In the baseline implementation, the demand component is assigned a weight of 0.60 and the residual-variability component a weight of 0.40. The resulting MPI field is shown in Fig. 5c. High-MPI zones indicate locations where elevated forecast demand coincides with higher updating variability. The MPI values have a mean of 0.419 and reach a maximum of 0.937, suggesting candidate areas for intensified monitoring or more detailed site-specific assessment.

Rank variability (Fig. 6) was also evaluated by ranking grid points according to their updated PGA values under each scenario and measuring the variability of these ranks across the scenario set. This indicator complements persistence and scenario sensitivity by distinguishing locations whose relative demand ranking remains stable from those whose relative importance changes with source configuration. Because rank variability provides a secondary interpretation of scenario dependence, it is retained as a supporting output rather than as a primary adaptation indicator.

Robustness checks were then performed for the demand threshold, priority-index weighting, and spatial concentration of high-demand zones. Threshold sensitivity shows that mean persistence decreases as the threshold becomes more restrictive, but maximum persistence remains 0.800 up to the p80 threshold and remains 0.600 at p90. This indicates that a core set of locations remains repeatedly critical even under stricter high-demand definitions.

The MPI weight-sensitivity results indicate that priority rankings remain highly stable when demand and residual variability are assigned comparable or demand-dominant weights. However, strongly uncertainty-dominant weighting substantially modifies the top-priority set. This suggests that the MPI can be adapted to different planning preferences while retaining stable priority structure for the baseline and balanced configurations.

As a compact spatial-organization check, connected-component analysis was also applied to the binary high-demand fields. At the p80 threshold, all five scenario fields produce high-demand domains dominated by a single connected component, with a largest component ratio of 1.000 in each case. The corresponding high-demand grid fractions are 0.141 for S1, 0.137 for S2, 0.429 for S3, 0.114 for S4,

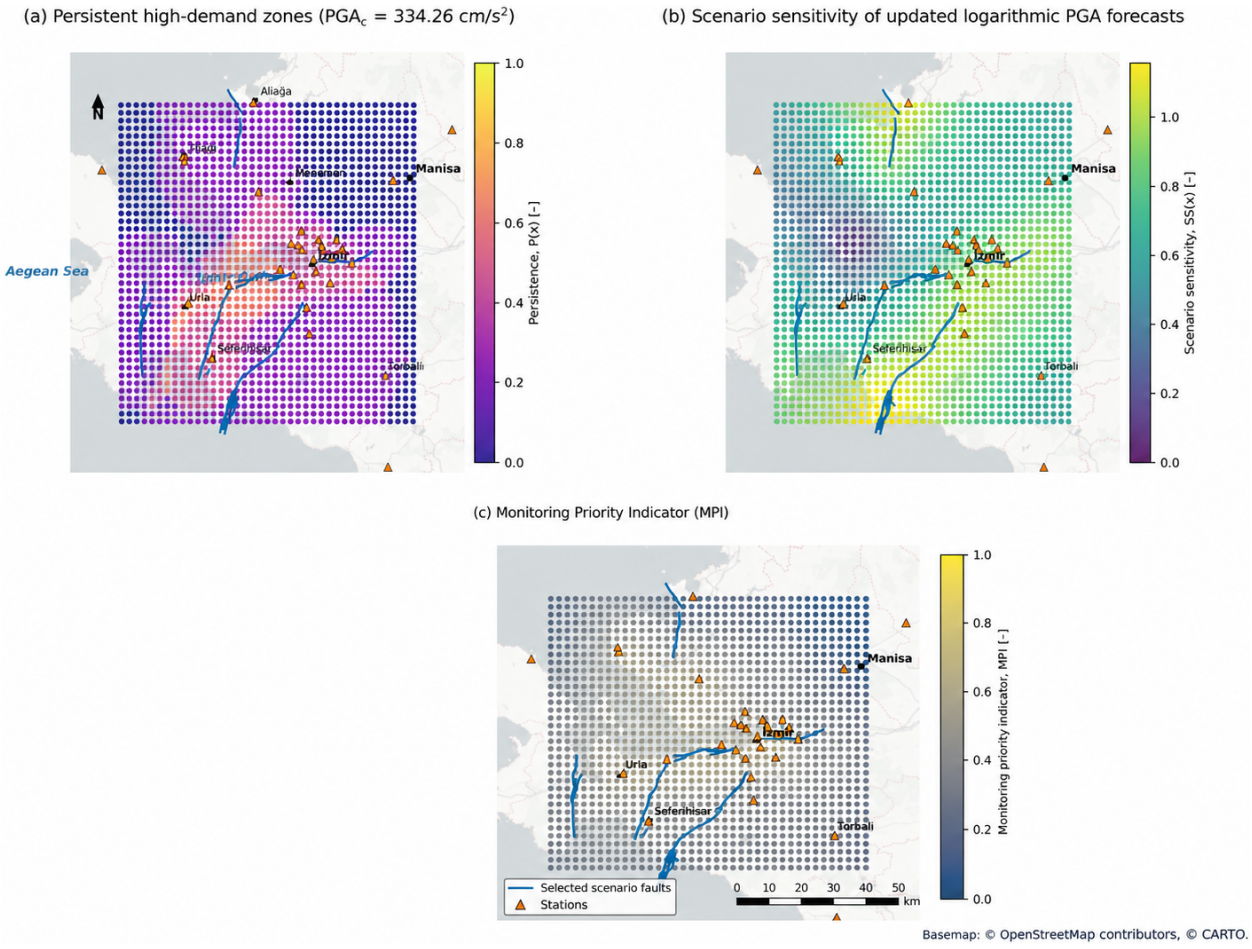


Figure 5. Adaptation-oriented spatial indicators derived from the monitoring-updated scenario forecasts: **(a)** persistent high-demand zones based on the common p80 threshold, $PGA_c = 334.26\,cm\,s^{-2}$; **(b)** scenario sensitivity of updated logarithmic PGA forecasts; and **(c)** Monitoring Priority Indicator (MPI) combining normalized updated demand and residual variability.

Table 7. Robustness summary for threshold selection and MPI weighting.

Test	Main result
Threshold sensitivity	Maximum persistence remains 0.800 up to p80 and 0.600 at p90
Fixed PGA thresholds	Maximum persistence reaches 1.000 at fixed thresholds of 150 and 200 $cm\,s^{-2}$
MPI 0.80/0.20	Spearman = 0.985; top-10 % overlap = 0.908
MPI 0.50/0.50	Spearman = 0.977; top-10 % overlap = 0.865
MPI 0.40/0.60	Spearman = 0.891; top-10 % overlap = 0.589
MPI 0.20/0.80	Spearman = 0.519; top-10 % overlap = 0.356

and 0.179 for S5. This indicates that high-demand zones form coherent exceedance regions rather than isolated grid-cell anomalies. This check is used here only as a supporting spatial concentration indicator within the resilience-oriented workflow.

Together, the persistence, scenario-sensitivity, MPI, rank-variability, and robustness outputs translate the monitoring-updated demand fields into adaptation-oriented spatial information. Persistent zones represent stable priorities across the scenario set, scenario-sensitive zones identify locations whose criticality depends on the assumed source configuration, and MPI highlights areas where elevated demand and residual variability coincide.

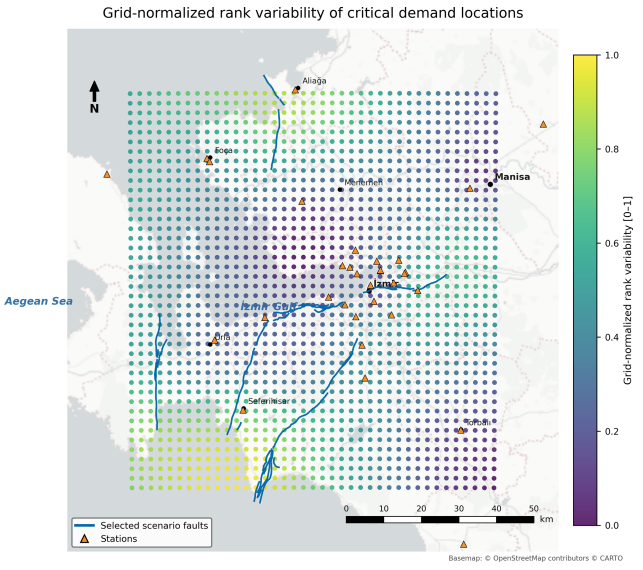


Figure 6. Rank variability of critical demand locations across the selected earthquake scenarios.

4.4 Digital-Twin-Oriented Updating and Uncertainty Propagation

To evaluate the updateability of the proposed workflow, the monitoring archive was divided into cumulative model versions ending in 2010, 2015, 2020, and 2025. For each version, the reference ground-motion representation, station-level residuals, spatial residual field, scenario forecasts, and monitoring-priority indicators were recomputed. This analysis evaluates how the monitoring-informed regional demand representation evolves as the observation archive expands. The model-version results are summarized in Table 8.

The number of usable records increases from 632 in the first version to 37 077 in the final version. The number of stations increases from 55 to 119, while the number of spatial-update stations increases from 19 to 108. Model performance also improves from the first to the final version, with RMSE decreasing from 0.937 to 0.801. The final two versions have very similar RMSE values, indicating that the reference representation becomes increasingly stable as the archive matures.

The sequential update log in Table 9 shows how the regional representation changes as new monitoring records are incorporated.

The largest changes occur in the earlier updates, when monitoring coverage and event sampling expand substantially. In contrast, the transition from v3 to v4 produces only minor changes. The residual-field delta RMSE decreases to 0.027, the MPI delta RMSE decreases to 0.011, the MPI rank correlation reaches 0.996, and the top-10 % priority overlap reaches 0.890. These results indicate that the monitoring-informed priority structure becomes highly stable in the final model version.

The same late-stage stabilization remained evident when station coverage was held fixed at 19 common stations across all model versions. For the 2020–2025 transition, the fixed-network analysis yielded a residual-field delta RMSE of 0.017, an MPI delta RMSE of 0.019, an MPI rank correlation of 0.995, and a top-10 % priority overlap of 0.840. This indicates that the observed stabilization is not solely attributable to expansion of the monitoring network.

The distinction between residual variability and correction uncertainty was also examined. Across the spatial-update stations, the mean event-to-event residual standard deviation was 0.705, whereas the mean standard error of the station-level correction was only 0.048. Over the prediction grid, the corresponding interpolated standard-error field had a mean of 0.032, substantially smaller than the mean residual-variability field of 0.663. The dominant scenario ranking remained unchanged when aleatory variability was considered separately from the combined predictive-dispersion formulation.

Uncertainty propagation was evaluated using Monte Carlo simulation of the predictive-dispersion field. For each scenario, 500 realizations were generated and exceedance probabilities were calculated relative to the p80 high-demand threshold, $\mathrm{PGA_c} = 334.26$. The Monte Carlo results are summarized in Table 10.

The Monte Carlo results confirm the deterministic scenario ranking. The Tuzla Fault scenario, S3, remains the dominant source configuration under predictive-dispersion propagation, with the highest mean exceedance probability of 0.452 and the largest fraction of grid points with $P_{\mathrm{exc}} > 0.50$, equal to 0.429. It also has the largest fraction of grid points with $P_{\mathrm{exc}} > 0.80$, equal to 0.162. The spatial distribution of $P_{\mathrm{exc},3}\,(x)$ for this scenario is shown in Fig. 7, where elevated exceedance probabilities form a broad footprint over the central and southern parts of the prediction domain. This probability pattern is consistent with the deterministic updated PGA forecast and the persistence structure obtained from the scenario ensemble.

Taken together, the digital-twin-oriented model-version tracking and Monte Carlo analyses extend the sense–forecast–adapt sequence from deterministic scenario mapping toward updateable and uncertainty-aware interpretation. The cumulative model versions indicate that the regional demand representation can be progressively revised as additional monitoring records become available, while the uncertainty propagation analysis illustrates how residual variability can be translated into probabilistic exceedance information. These results suggest that accumulated strong-motion observations can support an updateable, scenario-responsive, and adaptation-oriented spatial demand representation for proactive seismic resilience planning.

Table 8. Digital-twin-oriented model-version tracking.

Version	Period	Records	Stations	Events	(R^2)	RMSE	Spatial update stations	MPI mean	MPI max
v1	1977–2010	632	55	311	0.554	0.937	19	0.546	0.883
v2	1977–2015	4413	102	933	0.674	0.829	88	0.503	0.811
v3	1977–2020	29 906	117	2537	0.63	0.804	106	0.418	0.948
v4	1977–2025	37 077	119	2974	0.633	0.801	108	0.419	0.937

Table 9. Sequential update log for the digital-twin-oriented model versions.

Transition	Records added	Residual delta RMSE	MPI delta RMSE	MPI rank Spearman	Top 10 % MPI overlap
v1 → v2	3781	0.209	0.111	0.828	0.675
v2 → v3	25 493	0.171	0.122	0.825	0.558
v3 → v4	7171	0.027	0.011	0.996	0.89

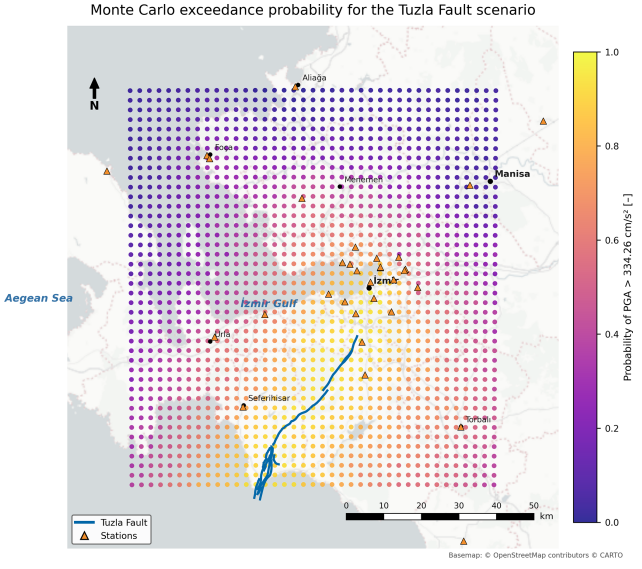


Figure 7. Monte Carlo exceedance-probability map for the Tuzla Fault scenario.

5 Discussion

The central implication of this study is the repositioning of strong-motion monitoring data from retrospective observation toward proactive scenario updating. Instead of using recorded motions only as event-specific measurements or post-event constraints, the proposed workflow converts station-level residual tendencies into a regional correction field that can modify future scenario-based PGA forecasts. This provides an updateable spatial demand representation in which accumulated monitoring records inform not only what has happened, but also how alternative future earthquake scenarios may be interpreted for resilience planning.

5.1 Field-Based Interpretation of Scenario Demand

Ground-motion prediction is commonly evaluated at individual sites, whereas regional resilience problems are inherently spatial. The results of this study indicate that the interpretation of seismic demand changes when the output is treated as a spatial field rather than as a set of independent station-level estimates. The selected scenarios differ not only in their mean and maximum PGA values, but also in the spatial extent and organization of elevated demand. The high-demand grid ratios show that the Tuzla Fault scenario generates the broadest high-demand footprint, followed by the Yenifoça Fault scenario, whereas the i˙, Seferihisar, and Gülbahçe scenarios produce more localized high-demand patterns. These source-dependent differences should be viewed within the broader tectonic setting of Türkiye, where rotation of the proposed deep structure has been linked to the accumulation of geodynamic stress, particularly in interpretations of the 2023 eastern Türkiye earthquake sequence (Eppelbaum et al., 2024). The relative scenario hierarchy should therefore be interpreted within the adopted representative magnitude and rupture-geometry assumptions rather than as a ranking of the intrinsic maximum seismic potential of the individual faults.

This finding is consistent with the broader literature on spatially correlated ground-motion fields. Previous studies have shown that spatial correlation of ground-motion residuals can significantly affect regional hazard and portfolio loss estimates because nearby sites do not respond independently during an earthquake (Jayaram and Baker, 2009). More recent studies further emphasize that spatial correlation may be influenced by source, path, and site effects, and that spatially coherent ground-motion fields are essential for regional seismic risk interpretation (Chen and Baker, 2019; Schiappapietra and Douglas, 2020; Bodenmann et al., 2023).

Table 10. Monte Carlo uncertainty propagation summary.

Scenario	Mean MC PGA	Max MC PGA	Mean exceedance probability	Max exceedance probability	Grid fraction ($P_{exc} > 0.50$)	Grid fraction ($P_{exc} > 0.80$)
S1	251.6	1194.83	0.218	0.854	0.142	0.007
S2	241.96	810.81	0.216	0.83	0.137	0.001
S3	487.48	2035.63	0.452	0.962	0.429	0.162
S4	194.43	823.95	0.155	0.808	0.115	0.001
S5	273.76	1307.11	0.225	0.944	0.179	0.053

The present study builds on this spatial-field perspective, but uses it in a forecasting-oriented manner. The objective is not to estimate a new spatial correlation model, but to update, compare, and interpret scenario-dependent demand fields for proactive resilience planning.

The connected-component results provide a supporting spatial-organization check within this field-based interpretation. At the $p80$ threshold, the high-demand regions are dominated by a main connected footprint rather than by isolated grid-cell anomalies. This supports the interpretation that the scenario forecasts produce spatially coherent high-demand domains. However, connectedness is used here only as a concentration indicator; a detailed analysis of fragmentation, spanning, or threshold-transition behavior is beyond the scope of the present study.

5.2 Role and Interpretation of the Residual Updating Layer

A central feature of the proposed framework is the use of monitoring-derived residuals as an updateable regional correction layer. The reference ground-motion representation provides a transparent baseline for estimating expected PGA from magnitude, source-to-site distance, and site-condition information. Station-level residuals then quantify systematic deviations between recorded and predicted motions. By interpolating these residual tendencies over the prediction domain, the monitoring archive is converted into a spatial correction field that can be combined with alternative future source scenarios.

This interpretation is closely related to recent developments in regionalized and non-ergodic ground-motion modelling. In such approaches, systematic source, path, and site effects are treated as spatially structured components rather than as purely random variability. Spatially varying coefficient models and non-ergodic ground-motion formulations have shown that allowing model terms to vary geographically can capture repeatable regional effects and reduce unexplained variability in ground-motion prediction (Landwehr et al., 2016; Lavrentiadis et al., 2023). Non-ergodic site-response studies similarly emphasize that local recordings can constrain systematic site effects and improve site-specific or region-specific ground-motion estimates (Stewart et al., 2017). The residual layer used in the present study follows the same general motivation: repeated observations are used to identify spatially persistent departures from a reference model.

The proposed implementation is intentionally simpler than a full non-ergodic ground-motion model. It does not decompose residuals into separate source, path, and site terms. Instead, it constructs a traceable regional correction surface that can be regenerated as the monitoring archive expands. This design is consistent with the broader idea of continuous model updating, in which ground-motion representations are revised as new observations become available rather than being treated as static models (Stafford, 2019). In the present workflow, updating occurs at the level of spatial residual correction: new strong-motion records can modify station-level residual tendencies, update the residual field, and revise the resulting scenario-based demand forecasts.

The leave-one-station-out validation indicates that station-level residual tendencies cannot be predicted with high precision from spatial position alone. This result defines the appropriate interpretation of the residual layer. It should not be viewed as a precise local residual predictor for individual stations. Rather, it functions as a low-bias regional correction layer that transfers accumulated monitoring information into scenario-based spatial demand forecasts.

The event-centered sensitivity analysis further supports this interpretation. Removal of event-specific mean residuals produced only minor changes in the residual surface and downstream scenario indicators, suggesting that the identified spatial correction pattern is not primarily an artifact of event-level residual offsets.

The additional simple-baseline comparison reinforces this interpretation, as spatial interpolation provides only modest pointwise predictive improvement, with the Gaussian-process benchmark showing the lowest cross-validated error. The spatial-block results further indicate that regional correction errors remain comparable under grouped spatial withholding, although local rank predictability deteriorates across larger monitoring gaps.

Importantly, the residual correction modifies demand levels without eliminating the primary influence of source configuration. The scenario hierarchy remains physically interpretable after updating, with the strongest demand patterns still governed by the assigned source magnitude, geometry,

and distance structure. The monitoring-derived layer therefore acts as an empirical regional adjustment to the source-controlled baseline fields, providing a practical basis for proactive seismic-demand screening.

5.3 Adaptation-Oriented Indicators for Proactive Resilience

The persistence, scenario-sensitivity, monitoring-priority, and rank-variability indicators constitute the adaptation-oriented layer of the proposed framework. Their main value is that they prevent the forecast ensemble from being reduced to a single deterministic PGA map. A single scenario map may identify where shaking is high under one assumed source, but it cannot distinguish between locations that are repeatedly critical, strongly source-dependent, uncertainty-influenced, or unstable in their relative priority. The proposed indicators make these distinctions explicit and therefore provide an intermediate decision-support layer between seismic monitoring and full regional risk assessment.

This interpretation is aligned with resilience-oriented planning. Seismic resilience is not limited to estimating physical damage; it also involves preparedness, consequence reduction, functionality preservation, and recovery. Bruneau et al. (2003) framed community seismic resilience in terms of reducing failure probabilities, reducing consequences, and reducing recovery time. In this context, the indicators developed here operate upstream of direct damage or loss estimation. They identify where elevated demand, source sensitivity, spatial concentration, and residual variability are located before exposure and vulnerability models are introduced.

The proposed workflow therefore complements, rather than replaces, full seismic risk platforms. It provides a demand-side screening layer that can help identify where more detailed vulnerability, exposure, or loss analyses should be prioritized. Such outputs may serve as input or preprocessing information for risk-oriented tools such as OpenQuake, which combine hazard, exposure, and vulnerability models for seismic risk calculation (Silva et al., 2014). In this sense, the framework supports proactive resilience planning by translating monitoring-informed scenario forecasts into spatially explicit prioritization information.

Accordingly, MPI should be interpreted as a demand-side monitoring and screening indicator; direct inspection prioritization would additionally require exposure, vulnerability, asset criticality, and consequence information.

5.4 Digital-Twin-Oriented Updating and Uncertainty-Aware Forecasting

The model-version tracking experiment provides the updateable component of the proposed workflow. Rather than treating the regional demand model as a static product, the framework allows the reference ground-motion representation, residual correction layer, residual-variability layer, scenario forecasts, and adaptation indicators to be regenerated as the monitoring archive expands. This creates a regional sensing-to-forecasting logic in which each cumulative model version represents an updated virtual description of spatial seismic demand.

This interpretation is consistent with recent developments in city, geospatial, and disaster-risk digital twins. City digital twins have been discussed as tools for urban resilience because they can integrate heterogeneous spatial data, support scenario exploration, and improve the communication of risk-relevant information to decision-makers (Therias and Rafiee, 2023). Disaster-risk twinning studies similarly emphasize dynamic data integration, virtual representation, uncertainty communication, and decision-support outputs for managing hazard-affected environments (Lagap and Ghaffarian, 2024; Wang and Wang, 2025).

The present study transfers this logic from individual structural assets to a regional seismic-demand field. The physical system is the İzmir Basin and its surrounding active-fault environment. The sensing layer is the strong-motion monitoring archive. The virtual representation consists of the reference ground-motion model, residual correction field, residual-variability layer, and scenario-based PGA fields. The updating mechanism is residual-based monitoring assimilation through cumulative model-version regeneration. The decision layer is represented by persistence, scenario sensitivity, monitoring priority, rank variability, spatial concentration, and exceedance-probability outputs. The correspondence between the proposed workflow and the main digital-twin components is summarized in Table 11.

As shown in Table 11, the proposed workflow should be interpreted as a digital-twin-oriented regional seismic-demand forecasting framework rather than as a fully operational real-time digital twin. It implements two core functions of a digital-twin logic: physical-to-virtual updating through monitoring-derived residual assimilation, and virtual-to-physical decision support through scenario forecasts and adaptation indicators. Real-time streaming, automated sensor-placement optimization, exposure/vulnerability coupling, and optimization-based intervention planning remain future operational extensions.

The sequential model-version results indicate that this virtual demand representation becomes more stable as the monitoring archive expands. The largest changes occur between earlier model versions, when the number of records and spatial-update stations increases substantially. In contrast, the transition from the 2020 version to the 2025 version produces only minor changes, with an MPI rank correlation of 0.996 and a top-10 % priority overlap of 0.890. This suggests that the monitoring-informed priority surface stabilizes as the observation archive matures.

The fixed-network analysis showed that late-stage stabilization persists even when station coverage is held constant, indicating that the accumulation of additional observations

Table 11. Digital-twin-oriented interpretation of the proposed monitoring-informed seismic-demand forecasting workflow.

Digital-twin component	Implementation in the present study
Physical system	İzmir Basin, surrounding active-fault environment, and regional strong-motion monitoring network
Sensing layer	Accumulated event–station strong-motion records, station metadata, and V_{s30} information
Digital/virtual system	Reference ground-motion representation, residual correction field, residual-variability field, and scenario-based PGA fields
Physical-to-virtual updating	Residual-based monitoring assimilation and cumulative model-version regeneration
Virtual-to-physical forecasting/decision support	Scenario PGA forecasts, persistence, scenario sensitivity, monitoring priority, rank variability, spatial concentration, and exceedance probability
Uncertainty representation	Residual-variability layer, Monte Carlo uncertainty propagation, and exceedance-probability mapping
Current optimization-related output	Monitoring priority and identification of high-demand or high-variability zones
Future operational extension	Event-based or near-real-time updating, sensor-placement optimization, exposure/vulnerability coupling, and intervention prioritization

contributes to convergence of the regional demand representation.

The Monte Carlo analysis extends the same framework into uncertainty-aware forecasting. The predictive-dispersion field is propagated into exceedance-probability maps, and the Tuzla Fault scenario remains the dominant source configuration under this uncertainty propagation. The agreement between deterministic ranking and Monte Carlo exceedance results indicates that the main scenario hierarchy is robust with respect to the adopted predictive-dispersion formulation. At the same time, exceedance-probability maps communicate the demand footprint in a form that is more directly interpretable for planning than deterministic PGA values alone.

Together, the model-version tracking and Monte Carlo analyses show how the proposed workflow can be updated and interpreted under uncertainty. New records can revise the residual correction layer, source scenarios can be re-evaluated, and adaptation indicators can be regenerated accordingly. This supports a basin-scale sense–forecast–adapt logic in which sensing updates the regional demand representation, forecasting evaluates alternative future demand states, and adaptation indicators support proactive resilience planning.

5.5 Limitations and Future Extensions

The present implementation prioritizes transparency, updateability, and interpretability. For this reason, the reference ground-motion representation is kept parsimonious and uses first-order predictors, including magnitude, source-to-site distance, and V_{s30}. This design makes the residual updating process traceable and reproducible, but it also limits the level of physical detail represented in the baseline model. Future extensions may incorporate more detailed source, path, and site terms, including basin-depth proxies, frequency-dependent site response, event-specific random effects, spatially varying coefficients, and non-ergodic adjustments.

The magnitude-range sensitivity analysis showed stable spatial demand patterns and scenario rankings across the tested calibration subsets, although absolute PGA levels varied with the magnitude composition of the dataset.

The residual correction layer should be interpreted as a regional screening and forecasting surface rather than as a precise local residual predictor. The leave-one-station-out validation indicates that station-level residual tendencies are difficult to reconstruct from spatial position alone, which is expected because residuals represent the remaining unexplained component after the main ground-motion predictors have been considered. Future implementations may improve this layer by incorporating geological units, basin geometry, station metadata, Bayesian hierarchical residual models, or Gaussian-process formulations with physically informed covariance structures.

The scenario sources are represented using mapped fault traces and a depth-adjusted distance proxy to enable consistent comparison among the selected source configurations. This representation is suitable for the scenario-comparison objective of the present study, but it does not capture the full complexity of earthquake rupture. Further developments may include finite-fault rupture geometry, directivity effects, hypocentre variability, rupture segmentation, magnitude–

rupture scaling uncertainty, and alternative source-distance metrics.

The uncertainty propagation analysis combines event-to-event residual variability with GP-based spatial prediction uncertainty and translates the resulting predictive-dispersion field into exceedance-probability maps. This provides an uncertainty-aware interpretation of the forecasted demand fields, but it does not exhaust the full uncertainty space. Future work may broaden the uncertainty treatment by incorporating alternative source models, epistemic uncertainty in ground-motion modelling, site-response uncertainty, and spatially correlated random-field simulations.

Future extensions may incorporate spatially correlated residual-field simulations when joint regional exceedance, connectivity, or portfolio-level consequences are of interest.

Finally, the adaptation-oriented indicators are intended to support screening, prioritization, and proactive planning, not to replace exposure, vulnerability, damage, or loss modelling. Direct integration with exposure, vulnerability, lifeline dependency, and recovery models would extend the workflow from spatial demand forecasting toward full resilience quantification. Such developments would allow the sense–forecast–adapt framework to support both early-stage regional prioritization and more detailed operational decision-support applications.

6 Conclusions

This study developed a monitoring-informed sense–forecast–adapt workflow for spatial seismic-demand forecasting in the İzmir Basin. The proposed framework converts accumulated strong-motion observations into a regional residual correction layer, embeds this layer within active-fault-based scenario forecasts, and translates the resulting demand fields into adaptation-oriented spatial indicators for proactive seismic resilience planning.

The results show that regional strong-motion observations can be used as an empirical updating layer for forward scenario forecasting. By aggregating event–station residuals at the station level and interpolating them over the prediction domain, the monitoring archive is transformed into a spatial correction surface that modifies scenario-based demand fields. The leave-one-station-out validation indicates that this residual surface should be interpreted as a regional correction layer rather than as a precise local residual predictor. Its main value lies in transferring accumulated monitoring information into spatial demand forecasts in a traceable and low-bias manner.

The scenario comparison highlights the importance of source configuration in controlling the spatial footprint of forecasted demand. Among the five scenario sources, the Tuzla Fault scenario consistently produces the strongest and broadest monitoring-updated demand pattern. The Yenifoça Fault scenario represents the main secondary demand case, whereas the i˙, Seferihisar, and Gülbahçe scenarios generate more localized high-demand patterns. These results support the use of multiple physically interpretable source scenarios when evaluating regional seismic-demand fields.

The adaptation-oriented indicators provide information beyond that available from deterministic PGA maps alone. Persistence, scenario sensitivity, monitoring priority, rank variability, and spatial concentration metrics distinguish locations that are repeatedly critical, source-dependent, uncertainty-influenced, or spatially coherent. The robustness analyses further indicate that the main spatial interpretations remain stable under reasonable changes in threshold selection and priority-index weighting, while the connected-component check shows that high-demand areas form coherent spatial footprints rather than isolated grid-cell anomalies.

The cumulative model-version experiment supports the updateable character of the workflow. As the monitoring archive expands, the residual and priority fields evolve and become increasingly stable in the most recent model versions. This provides a digital-twin-oriented interpretation of the framework, in which the regional virtual demand representation can be revised as new strong-motion records become available. The Monte Carlo simulations further extend the workflow into uncertainty-aware forecasting by translating predictive dispersion into exceedance-probability maps. The resulting probabilistic outputs preserve the main deterministic scenario hierarchy, with the Tuzla Fault scenario remaining the dominant source configuration.

Overall, the study shows that monitoring-derived residual updating, scenario-based demand forecasting, adaptation-oriented indicators, model-version tracking, and exceedance-probability mapping can be integrated into a single field-based workflow. The proposed approach provides an updateable basis for identifying persistent, source-sensitive, spatially coherent, and uncertainty-influenced seismic-demand zones in monitored basin environments. In this form, the workflow can support proactive seismic resilience planning by linking regional monitoring archives with future scenario evaluation and spatial decision-support indicators.

Code and data availability. All data and models analyzed during the current study are available from the corresponding author on reasonable request.

Author contributions. Ş. Ç. Tuna conceived and designed the study, performed the analyses, interpreted the results, prepared the figures, and wrote and revised the manuscript.

Competing interests. The contact author has declared that none of the authors has any competing interests.

Disclaimer. Publisher's note: Copernicus Publications remains neutral with regard to jurisdictional claims made in the text, published maps, institutional affiliations, or any other geographical representation in this paper. The authors bear the ultimate responsibility for providing appropriate place names. Views expressed in the text are those of the authors and do not necessarily reflect the views of the publisher.

Acknowledgements. The author gratefully acknowledges the Disaster and Emergency Management Presidency (AFAD) of Türkiye for providing access to the strong-motion records used in this study.

Financial support. This research was supported by Yaşar University Scientific Research Project (BAP) Program (project no. BAP148), titled "Application of Artificial Intelligence to Enhance Seismic Hazard Maps and Risk Mitigation Strategies in Izmir".

Review statement. This paper was edited by Lev Eppelbaum and reviewed by two anonymous referees.

References

Bodenmann, L., Baker, J. W., and Stojadinović, B.: Accounting for path and site effects in spatial ground-motion correlation models using Bayesian inference, Nat. Hazards Earth Syst. Sci., 23, 2387–2402, https://doi.org/10.5194/nhess-23-2387-2023, 2023.

Bruneau, M., Chang, S. E., Eguchi, R. T., Lee, G. C., O'Rourke, T. D., Reinhorn, A. M., Shinozuka, M., Tierney, K., Wallace, W. A., and von Winterfeldt, D.: A framework to quantitatively assess and enhance the seismic resilience of communities, Earthq. Spectra, 19, 733–752, https://doi.org/10.1193/1.1623497, 2003.

Campbell, K. W. and Bozorgnia, Y.: NGA-West2 ground motion model for the average horizontal components of PGA, PGV, and 5 % damped linear acceleration response spectra, Earthq. Spectra, 30, 1087–1115, https://doi.org/10.1193/062913EQS175M, 2014.

Chen, Y. and Baker, J. W.: Spatial correlations in CyberShake physics-based ground motion simulations, Bull. Seismol. Soc. Am., 109, 2447–2458, https://doi.org/10.1785/0120190065, 2019.

Coşkun, S., Dondurur, D., Çifçi, G., Aydemir, A., Güngör, T., and Drahor, M. G.: Investigation on the tectonic significance of i˙, Uzunada Fault Zones and other tectonic elements in the Gulf of i˙, western Turkey, using high resolution seismic data, Mar. Petrol. Geol., 83, 73–83, https://doi.org/10.1016/j.marpetgeo.2017.03.010, 2017.

Du, A. and Padgett, J. E.: Post-event regional seismic risk assessment via vector-IM-based record updating, in: Bridge Maintenance, Safety, Management, Life-Cycle Sustainability and Innovations, edited by: Yokota, H. and Frangopol, D. M., CRC Press, 586, https://doi.org/10.1201/9780429279119-375, 2021.

Emre, Ö., Duman, T. Y., Özalp, S., Şaroğlu, F., Olgun, Ş., Elmacı, H., and Çan, T.: Active fault database of Turkey, Bull. Earthq. Eng., 16, 3229–3275, https://doi.org/10.1007/s10518-016-0041-2, 2018.

Engler, D. T., Thompson, E. M., Maurer, B. W., Geyin, M., Burgi, P. M., Allstadt, K., and Jaiswal, K. S.: Updating regional-scale geospatial liquefaction models with locally available geotechnical data, Seismol. Res. Lett., 96, 3365–3378, https://doi.org/10.1785/0220250134, 2025.

Eppelbaum, L. V., Ben-Avraham, Z., Katz, Y. I., Cloetingh, S., and Kaban, M. K.: Giant quasi-ring mantle structure in the African–Arabian junction: Results derived from the geological–geophysical data integration, Geotectonics, 55, 58–82, https://doi.org/10.1134/S0016852121010052, 2021.

Eppelbaum, L. V., Katz, Y. I., and Ben-Avraham, Z.: The reasons for enormous accumulation of the geodynamic tension in Eastern Turkey: A multidisciplinary study, Geol. Geophys. Earth Sci., 2, 1–28, https://doi.org/10.58396/gges020202, 2024.

Eppelbaum, L. V., Katz, Y. I., and Ben-Avraham, Z.: Giant quasi-ring mantle structure beneath the Eastern Mediterranean: Interpretation of new seismic tomography, magnetic field, and paleobiogeographic data, Geotectonics, 59, 101–126, https://doi.org/10.1134/S001685212570013X, 2025.

Goda, K. and Atkinson, G. M.: Probabilistic characterization of spatially correlated response spectra for earthquakes in Japan, Bull. Seismol. Soc. Am., 99, 3003–3020, https://doi.org/10.1785/0120090007, 2009.

Huang, D. and Wang, G.: Region-specific spatial cross-correlation model for stochastic simulation of regionalized ground-motion time histories, Bull. Seismol. Soc. Am., 105, 272–284, https://doi.org/10.1785/0120140198, 2015.

Jayaram, N. and Baker, J. W.: Correlation model for spatially distributed ground-motion intensities, Earthq. Eng. Struct. Dyn., 38, 1687–1708, https://doi.org/10.1002/eqe.922, 2009.

Kaklamanos, J., Baise, L. G., and Boore, D. M.: Estimating unknown input parameters when implementing the NGA ground-motion prediction equations in engineering practice, Earthq. Spectra, 27, 1219–1235, https://doi.org/10.1193/1.3650372, 2011.

Kwak, D. Y. and Ahn, J.-K.: Update of mainshock intensity map using aftershock records collected from temporary seismic stations: Case study of 2017 M5.4 Pohang earthquake, Earthq. Spectra, 42, https://doi.org/10.1002/esp4.70048, 2026.

Lagap, U. and Ghaffarian, S.: Digital post-disaster risk management twinning: A review and improved conceptual framework, Int. J. Disaster Risk Reduct., 110, 104629, https://doi.org/10.1016/j.ijdrr.2024.104629, 2024.

Landwehr, N., Kuehn, N. M., Scheffer, T., and Abrahamson, N. A.: A nonergodic ground-motion model for California with spatially varying coefficients, Bull. Seismol. Soc. Am., 106, 2574–2583, https://doi.org/10.1785/0120160118, 2016.

Lavrentiadis, G., Abrahamson, N. A., Kuehn, N. M., Bozorgnia, Y., Goulet, C. A., Babič, A., Macedo, J., Dolšek, M., Gregor, N., Kottke, A. R., Lacour, M., Liu, C., Meng, X., Phung, V.-B., Sung, C.-H., and Walling, M.: Overview and introduction to development of non-ergodic earthquake ground-motion models, Bull. Earthq. Eng., 21, 5121–5151, https://doi.org/10.1007/s10518-022-01485-x, 2023.

Loth, C. and Baker, J. W.: A spatial cross-correlation model of ground motion spectral accelerations at multiple periods, Earthq. Eng. Struct. Dyn., 42, 397–417, https://doi.org/10.1002/eqe.2212, 2013.

Özener, H., Doğru, A., and Acar, M.: Determination of the displacements along the Tuzla Fault, Aegean Region–Turkey: Preliminary results from GPS and precise leveling techniques, J. Geodyn., 67, 13–20, https://doi.org/10.1016/j.jog.2012.06.001, 2013.

Schiappapietra, E. and Douglas, J.: Modelling the spatial correlation of earthquake ground motion: Insights from the literature, data from the 2016–2017 Central Italy earthquake sequence and ground-motion simulations, Earth-Sci. Rev., 203, 103139, https://doi.org/10.1016/j.earscirev.2020.103139, 2020.

Silva, V., Crowley, H., Pagani, M., Monelli, D., and Pinho, R.: Development of the OpenQuake engine, the Global Earthquake Model's open-source software for seismic risk assessment, Nat. Hazards, 72, 1409–1427, https://doi.org/10.1007/s11069-013-0618-x, 2014.

Stafford, P. J.: Continuous integration of data into ground-motion models using Bayesian updating, J. Seismol., 23, 39–57, https://doi.org/10.1007/s10950-018-9792-3, 2019.

Stewart, J. P., Afshari, K., and Goulet, C. A.: Non-ergodic site response in seismic hazard analysis, Earthq. Spectra, 33, 1385–1414, https://doi.org/10.1193/081716EQS135M, 2017.

Şengöçmen Geçkin, B., Sözbilir, H., Özkaymak, Ç., and Softa, M.: Active tectonics of Gülbahçe Fault Zone (GBFZ) by using geomorphic indices, İzmir Province, western Anatolia, Turkey, Afyon Kocatepe Univ. J. Sci. Eng., 21, 1195–1209, https://doi.org/10.35414/akufemubid.946298, 2021.

Tamhidi, A., Kuehn, N. M., Ghahari, S. F., Rodgers, A. J., Kohler, M. D., Taciroglu, E., and Bozorgnia, Y.: Conditioned simulation of ground-motion time series at uninstrumented sites using Gaussian process regression, Bull. Seismol. Soc. Am., 112, 331–347, https://doi.org/10.1785/0120210054, 2022.

Thelen, A., Zhang, X., Fink, O., Lu, Y., Ghosh, S., Youn, B. D., Todd, M. D., Mahadevan, S., Hu, C., and Hu, Z.: A comprehensive review of digital twin – part 1: Modeling and twinning enabling technologies, Struct. Multidiscip. Optim., 65, 354, https://doi.org/10.1007/s00158-022-03425-4, 2022.

Thelen, A., Zhang, X., Fink, O., Lu, Y., Ghosh, S., Youn, B. D., Todd, M. D., Mahadevan, S., Hu, C., and Hu, Z.: A comprehensive review of digital twin – part 2: Roles of uncertainty quantification and optimization, a battery digital twin, and perspectives, Struct. Multidiscip. Optim., 66, 1, https://doi.org/10.1007/s00158-022-03410-x, 2023.

Therias, A. and Rafiee, A.: City digital twins for urban resilience, Int. J. Digit. Earth, 16, 4164–4190, https://doi.org/10.1080/17538947.2023.2264827, 2023.

Torzoni, M., Tezzele, M., Mariani, S., Manzoni, A., and Willcox, K. E.: A digital twin framework for civil engineering structures, Comput. Method. Appl. M., 418, 116584, https://doi.org/10.1016/j.cma.2023.116584, 2024.

Vanmarcke, E. H. and Fenton, G. A.: Conditioned simulation of local fields of earthquake ground motion, Struct. Saf., 10, 247–264, https://doi.org/10.1016/0167-4730(91)90018-5, 1991.

Vanmarcke, E. H., Heredia-Zavoni, E., and Fenton, G. A.: Conditional simulation of spatially correlated earthquake ground motion, J. Eng. Mech., 119, 2333–2352, https://doi.org/10.1061/(ASCE)0733-9399(1993)119:11(2333), 1993.

Viallet, E., Humbert, N., and Mottier, P.: Updating a probabilistic seismic hazard assessment with instrumental and historical observations based on a Bayesian inference, Nucl. Eng. Des., 350, 112–127, https://doi.org/10.1016/j.nucengdes.2019.04.034, 2019.

Wang, Z. and Wang, Z.: Risk twin: Real-time risk visualization and control for structural systems, Struct. Multidiscip. Optim., 68, 85, https://doi.org/10.1007/s00158-025-04014-x, 2025.

Wells, D. L. and Coppersmith, K. J.: New empirical relationships among magnitude, rupture length, rupture width, rupture area, and surface displacement, Bull. Seismol. Soc. Am., 84, 974–1002, 1994. https://doi.org/10.1785/BSSA0840040974

Worden, C. B., Wald, D. J., Allen, T. I., Lin, K., Garcia, D., and Cua, G.: A revised ground-motion and intensity interpolation scheme for ShakeMap, Bull. Seismol. Soc. Am., 100, 3083–3096, https://doi.org/10.1785/0120100101, 2010.